DYNAMICAL AND PHOTOMETRIC INVESTIGATION OF COMETARY TYPE II TAILS

Grant NGR 09-015-159

Semiannual Progress Report No. 6

For the period March 15 to September 14, 1974

Principal Investigator

Dr. Zdenek Sekanina

Prepared for

National Aeronautics and Space Administration

Washington, D.C. 20546

Smithsonian Institution
Astrophysical Observatory
Cambridge, Massachusetts 02138

DYNAMICAL AND PHOTOMETRIC INVESTIGATION OF COMETARY TYPE II TAILS

Grant NGR 09-015-159

Semiannual Progress Report No. 6

For the period March 15 to September 14, 1974

Principal Investigator

Dr. Zdenek Sekanina

Prepared for

National Aeronautics and Space Administration

Washington, D.C. 20546

Smithsonian Institution
Astrophysical Observatory
Cambridge, Massachusetts 02138

TABLE OF CONTENTS

ABSTRACT

Photographic observations of the antitail of Comet Kohoutek (1973f), obtained by F. D. Miller, University of Michigan, at the Cerro Tololo Interamerican Observatory, are photometrically studied and the results compared with the working model of the antitail, formulated by the writer. The applied technique of photometric reduction is described and the radial and transverse profiles of the antitail, corrected for the effects of the variable intensity of the sky background, are derived. The most important result reached so far is a quantitative confirmation of the previously suggested hypothesis, arguing that dust particles in the antitail suffered a significant loss in radius due to evaporation near the perihelion passage. We find that only particles initially larger than 0.1 to 0.15 mm in diameter (at an assumed density 1 g cm^{-3}) survived. Numerically, however, this result is still tentative, because the dynamical effect exerted by particle evaporation remains to be accounted for.

Other activities undertaken in the reported period are also mentioned, and the plans for the next semiannual period are briefly listed.

PART A. COMPARISON OF THE WORKING MODEL FOR THE ANTITAIL OF COMET KOHOUTEK (1973f) WITH GROUND-BASED PHOTOGRAPHIC OBSERVATIONS

I. Introduction

A working model has recently been formulated for the antitail of Comet Kohoutek (Sekanina 1974, referred to hereafter as Paper I; see also Semiannual Report No. 5). The model is based on the Finson-Probstein (1968) theory of dust comets and fits reasonably well the semiquantitative descriptions of the antitail by a number of observers. Yet some fundamental tests of the working model of the antitail, such as radial brightness variations, transverse profiles and time variations in the surface brightness, were missing in Paper I because quantitative photometry was unavailable at the time of the paper's completion. Some of these tests are included in the present report.

The photographic material studied here consists of the plates secured at the Cerro Tololo Interamerican Observatory, near La Serena, Chile, under the supervision of F. D. Miller.

II. The Cerro Tololo photographs

A total of 12 plates were taken at Cerro Tololo with the University of Michigan Curtis-Schmidt telescope (61/91 cm, f/3.5, 96".6 per millimeter) between January 16 and February 15, 1974. Five plates, taken on January 23, 24, 26 and on February 12 and 15, are 098-02 panchromatic emulsions combined with an RG1 filter to provide the maximum sensitivity near 6600Å. The other seven plates, taken on January 16, 17, 20, 21, 23, 25 and 27, are standard

103a0 emulsions without any filter. All the plates were calibrated with the use of 14 photometric spots from the Weston tube sensitometer.

The red-sensitive plates have been of primary interest, both because of their spanning a longer interval of time and because of their better showing the antitail. The guiding of the January 24 plate was somewhat imperfect, so that only the remaining four plates - two in January and two in February - have been photometrically studied. The four observations are listed in Table I.

Of much concern is of course the very low altitude of the comet. At the end of the exposure, the comet was only slightly over 10° above the horizon on plates 15520, 15687 and 15703, and about 6°.5 above the horizon on 15554! Only thanks to the excellent sky at Cerro Tololo the plates are still photometrically valuable. Yet the very low altitude of the comet is a source of two potential complications for the photometry of the plates, namely the effects of differential refraction and strongly variable sky brightness.

The effect of differential refraction has been quantitatively analyzed following the procedure described in Appendix A. Numerically, refraction has been found to affect the angular distance from the nucleus on the four plates by less than 1%, and the positional angle by not more than 0°.1 at the angular distance of 1° from the nucleus and not more than 0°.2 at 2°.

The effect of variable sky brightness proved considerably more severe. It so happened that the brightest section of the antitail directed almost exactly toward the horizon on all the plates, so that the maximum brightness gradient of the sky projected unforeshortened along the antitail. In addition,

Table I. Cerro Tololo red-sensitive photographs of Comet Kohoutek (098-02 emulsion with an RG1 filter)

Plate	Date UT 1974	Comet's position 1950.0 R.A.	Decl.	Δ (a.u.)	r (a.u.)	Phase angle α	Altitude at midexposure	Exposure (min)
15520	Jan. 23.0495	$23^h40^m.67$	+ 0°46'.5	0.853	0.837	71°.2	13°.6	20
15554	Jan. 26.0614	0 07.30	+ 3 12.2	0.894	0.909	66.2	11.8	50
15687	Feb. 12.0572	1 54.21	+12 01.9	1.257	1.278	45.8	16.3	60
15703	Feb. 15.0566	2 07.40	+12 57.7	1.334	1.338	43.4	16.2	60

all exposures began still during the astronomical twilight (with the sun's depression between 15° and 17°), and almost the whole 15520 exposure was taken during the twilight (the sun's depression at midexposure 17°). To demonstrate the extent of interference, we mention that the relative gradient of the sky brightness on plates 15520 and 15554 reached a record rate of 7 per cent per degree of altitude, while at the same time the intrinsic surface brightness of the antitail amounted to only some 4 - 6% of the sky brightness at 15 arcmin from the nucleus and about 1 - 2% at 25 arcmin.

III. Photographic photometry of the Cerro Tololo plates. The technique

The technique of reduction of the Cerro Tololo plates has essentially been dictated by the troublesome observing conditions. Because of the complicated character of the sky-brightness variations near the horizon, it has been virtually impossible to use the standard two-dimensional scans to map the background "noise" over the area occupied by the antitail (see Fig. 1). Preferable - because considerably more revealing - are one-dimensional radial tracings, passing through the comet's nucleus and effectively covering the whole antitail. Each radial scan is defined by the positional angle, and the "noise" variations in the respective section of the antitail can reasonably be interpolated from the known background outside the antitail (see Fig. 2). Nearby stars of known positions have been used to fix the positional angles. The position of the comet on the plates was measured relative to the nearby stars and reduced routinely with the use of the method of dependences. The result has also been checked by computing the expected position of the comet

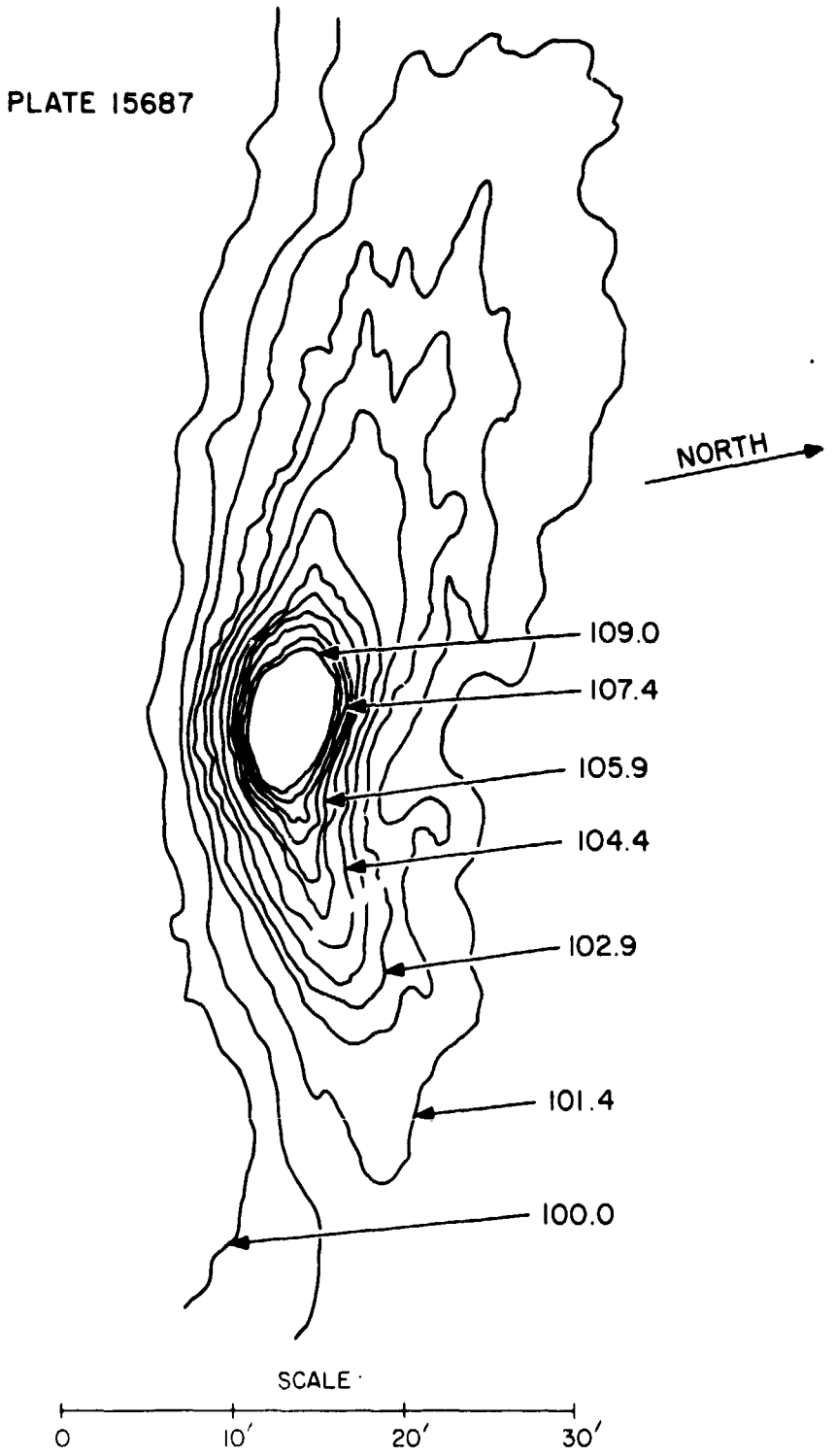

Figure 1. A two-dimensional scan of Plate 15687. Scanning aperture 9.7 by 9.7 arcsec. The antitail points to the bottom, the regular dust tail to the top of the scan. The numbers indicate the relative surface brightness, uncorrected for the sky background.

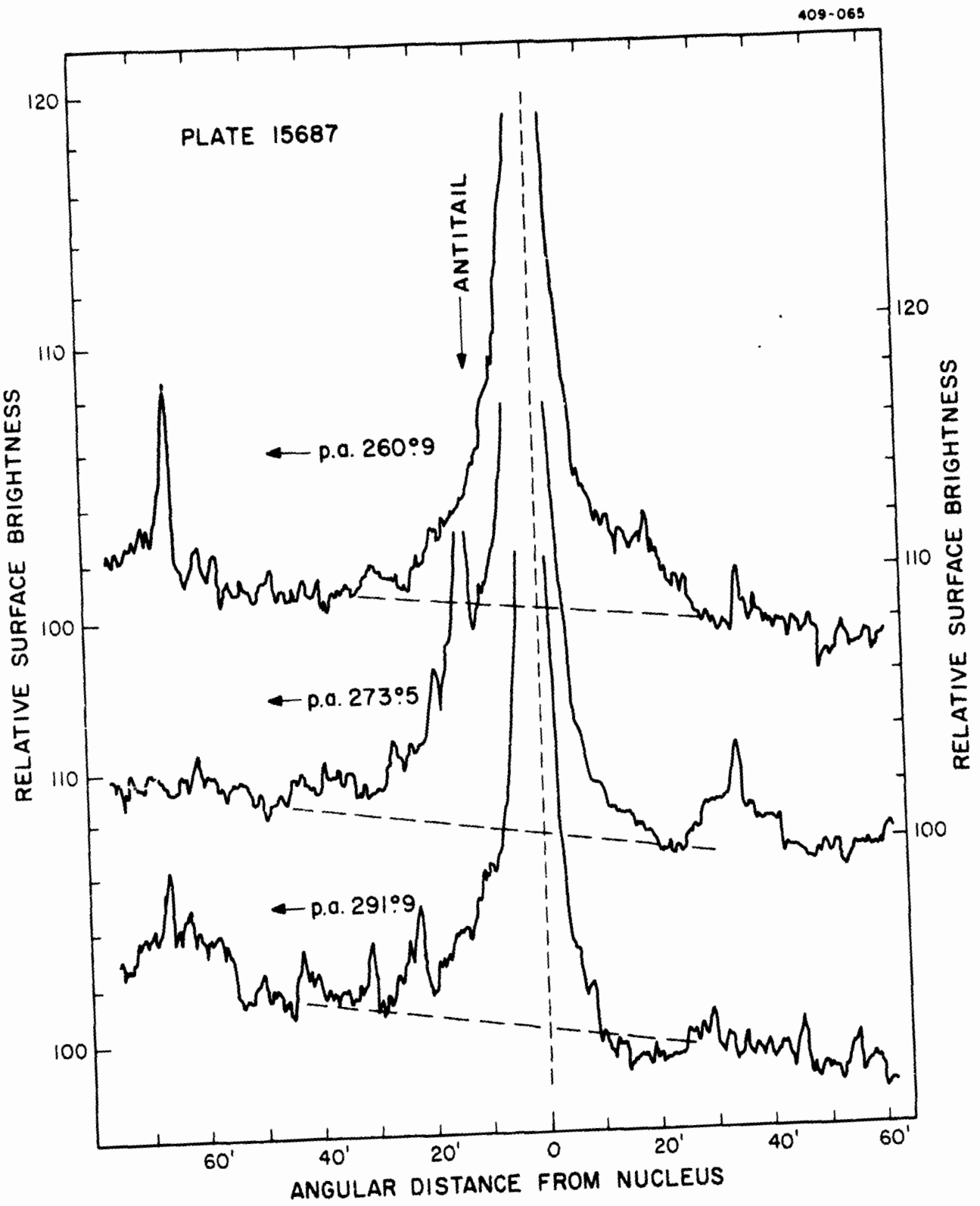

Figure 2. Three radial scans of Plate 15687. Scanning aperture 5.8 by 5.8 arcsec. Note the variable sky brightness (dashed curves).

from Marsden's (1974) definitive orbit. The measured and computed positions agree within 2 arcsec on plate 15520, 7 arcsec on 15554, 8 arcsec on 15687 and 13 arcsec on 15703. These residuals can entirely be accounted for by the uncertainty in the location on the plates of the nucleus in the strongly overexposed coma of almost 2 arcmin in diameter. The extended image of the comet's head is responsible for an uncertainty in the distance scale of the scans, amounting to several per cent at 10 arcmin from the nucleus and dropping down to somewhat more than 1 per cent at 30 arcmin. Together with the images of the orientation-fixing stars, which appear as trails a few arcmin in length on the four plates, the comet's image is also responsible for an error in the positional angle of the scans, which is estimated at not more than about $\pm 0^{\circ}.5$. Recalling the effects introduced by differential refraction (Section II), we may conclude that they are much smaller than the operating errors and can therefore be safely neglected.

A practically important parameter of any photometric procedure is the size of the scanning diaphragm. Its choice is governed by a balanced compromise between the requirement of a sufficiently high resolution power on the one hand and that of a smooth background image reasonably free from the effects of emulsion granulation on the other. After some experimenting, the diaphragm used in the radial scans was fixed at 60 by 60 microns, i.e., 5.8 by 5.8 arcsec.

The photoelectrically calibrated spots have been measured with a Macbeth densitometer. The obtained characteristic curves are plotted in Fig. 3.

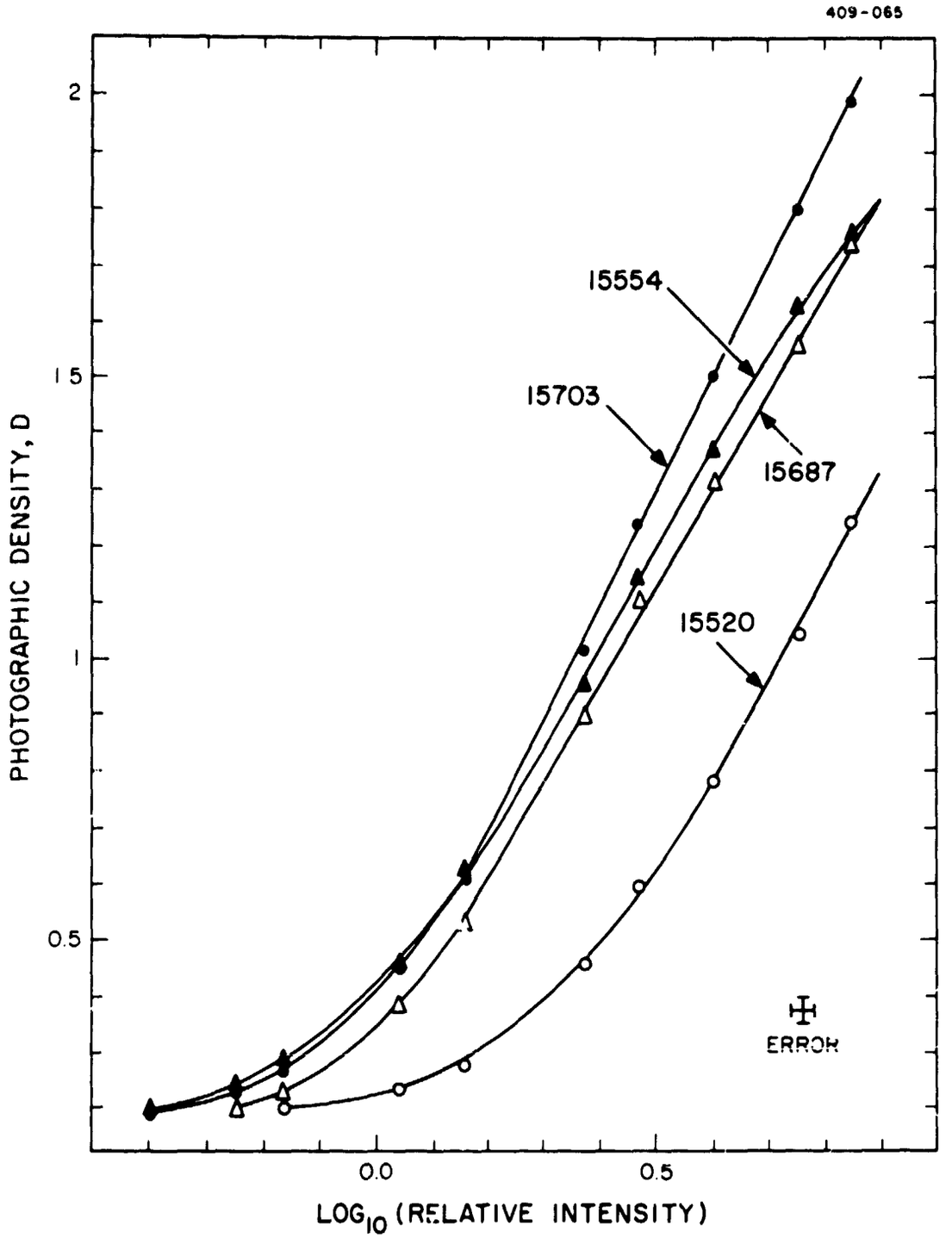

Figure 3. The characteristic curves for the four Cerro Tololo plates.

IV. Photographic photometry of the Cerro Tololo plates. The results

The photometric procedure described in Section III has been applied to the four Cerro Tololo plates and the results are listed in Tables II to V. The smoothed brightness data are missing for areas of the antitail where its photographic-density curve is very poorly determined, either because of the excessive faintness of the antitail or due to a strong interference with a star's trail.

The data of Tables II to V have been first compared with the radial profiles of the working model (Fig. 4D of Paper I). All four plates consistently show the effect displayed in Fig. 4 for one of the scans of Table II: the observed radial gradient progressively increases with distance from the nucleus. The surface brightness varies approximately in inverse proportion to the distance from the nucleus at angular distances less than about 10', and approaches the model's inverse 2.8 power law at about a half of a degree from the nucleus. The quantitative dependence of the radial gradient on the angular distance varies somewhat with the positional angle and to some extent also changes from plate to plate. Since the adopted assumption of negligibly small emission velocities implies a close correlation between the radial variation of the brightness in the antitail and the population index s of the particle mass distribution $m^{-s}\,dm$, the observed character of the radial gradient suggests a strongly variable s in the particle-size range under consideration, a case that has not been discussed in Paper I.

Although the variability of the radial gradient makes further comparison of the working model with our photometric results rather difficult, we have

Table II. Surface brightness of the antitail on plate 15520

Surface brightness of 100 units = photographic density 0.42
Sky brightness at the nucleus = 103.5 units

Angular distance from nucleus (arcmin)	Surface brightness in positional angle								
	255°.8	263°.4	269°.1	275°.5	279°.7	288°.1	293°.2	301°.1	318°.8
4.03	18.5	20.8	23.6	22.6	22.4	20.1	19.7	19.3	16.3
5.64	12.9	15.2	16.4	15.7	16.1	14.5	14.4	13.8	10.8
8.05	8.5	10.1	11.0	10.3	11.1	9.7	10.1	9.1	6.5
11.27	5.6	6.3	7.2	6.6	6.5	5.9	6.3	5.4	3.7
15.30	3.6	3.7	4.0	3.7	3.5	3.1	3.6	2.8	1.8
20.13	2.2	2.2	2.2	2.2	1.9	1.6	1.9	1.4	0.9
24.96	.	1.4	1.3	1.2	1.1	0.9	1.0	0.8	.

Table III. Surface brightness of the antitail on plate 15554

Surface brightness of 100 units = photographic density 0.60
Sky brightness at the nucleus = 100.4 units

Angular distance from nucleus (arcmin)	Surface brightness in positional angle						
	266°.6	276°.3	285°.3	296°.8	302°.8	308°.8	314°.8
4.03	.	.	.	.	29.0	27.4	25.3
5.64	.	.	.	.	21.1	20.1	18.5
8.05	21.7	24.6	22.7	13.2	13.5	11.5	10.5
11.27	13.6	15.2	13.4	8.3	8.3	6.6	6.1
15.30	6.2	8.7	6.9	4.9	4.2	3.4	3.2
20.13	3.0	4.7	3.6	2.7	2.1	1.7	1.5
24.96	1.4	2.8	2.1	1.6	.	.	.
30.59	0.6	1.7	1.2	0.9	.	.	.

Table IV. Surface brightness of the antitail on plate 15687

Surface brightness of 100 units = photographic density 0.90
Sky brightness at the nucleus = 100.4 units

Angular distance from nucleus (arcmin)	Surface brightness in positional angle								
	260°.9	264°.1	268°.0	271°.6	273°.5	279°.0	283°.4	287°.6	291°.9
4.03	13.7	13.3	15.4	15.8	17.2	15.7	15.4	13.1	11.8
5.64	10.0	10.3	12.0	12.3	13.5	12.3	12.1	10.1	8.5
8.05	6.5	7.2	8.4	8.9	9.9	8.9	8.5	7.1	5.8
11.27	4.3	5.0	5.6	5.9	7.1	6.2	5.8	4.7	3.6
15.30	2.7	3.3	3.5	3.9	4.7	4.0	3.6	2.9	2.1
20.13	1.6	.	2.0	2.4	3.0	2.4	2.1	1.6	1.2
24.96	.	.	1.3	1.7	2.1	1.6	1.4	1.0	0.8
30.59	.	.	0.9	1.1	1.4	1.1	0.9	0.6	0.5
37.03	.	.	0.6	0.8	0.9	0.7	0.6	.	.

Table V. Surface brightness of the antitail on plate 15703

Surface brightness of 100 units = photographic density 0.80
Sky brightness at the nucleus = 101.6 units

Angular distance from nucleus (arcmin)	Surface brightness in positional angle							
	264°.2	269°.2	274°.8	277°.7	281°.4	286°.7	292°.0	296°.0
4.03	15.5	16.1	17.7	16.0	15.7	14.7	13.4	12.8
5.64	12.6	13.3	14.0	12.8	12.8	11.7	10.8	10.0
8.05	9.5	10.3	10.4	9.7	9.9	8.7	7.9	7.3
11.27	6.8	7.4	7.4	6.9	7.1	6.0	5.3	4.9
15.30	4.6	4.9	5.0	4.6	4.8	3.8	3.3	3.0
20.13	2.8	3.1	3.2	2.9	2.9	2.3	2.0	1.7
24.96	1.8	2.0	2.1	2.0	1.8	1.4	1.2	1.0
30.59	1.2	1.3	1.4	1.3	1.2	0.9	0.8	0.6
37.03	0.7	0.9	0.9	0.8	0.7	0.6	0.5	0.4

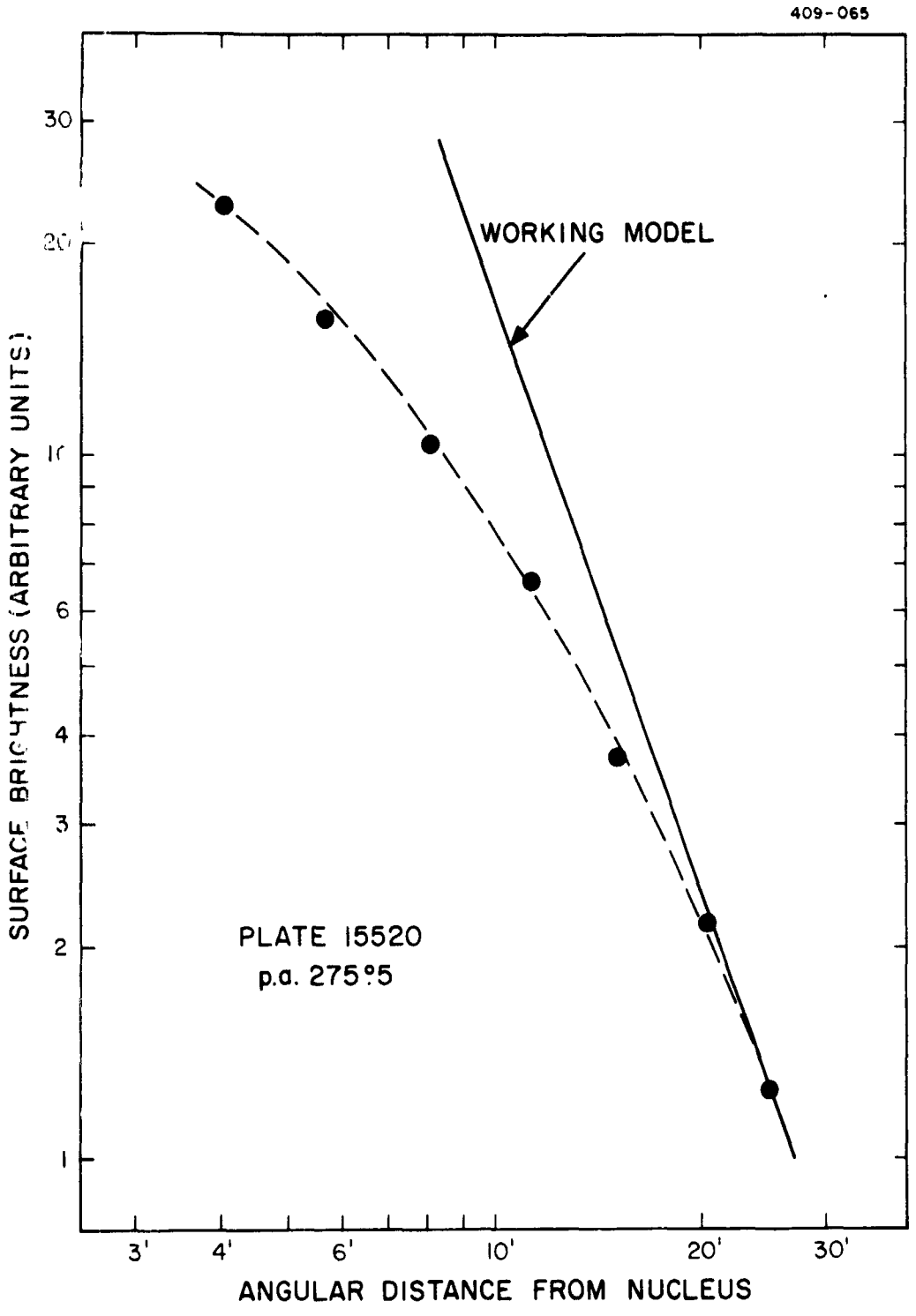

Figure 4. A typical example of the radial variation in the antitail brightness (solid circles). The law of variation derived from the working model is given for reference.

used some of the data of Tables II to V to compile Figure 5. It shows the profiles of the antitail at 20 arcmin from the nucleus, as a function of positional angle. The general impression from the comparison of the observations with the working model is that the antitail appears to be, primarily in February, broader than anticipated. When an attempt has been made to force the 2.8 power law through the brightness curve of the antitail near 30 arcmin from the nucleus, the agreement with the working model's transverse profiles became substantially better. However, since the brightness data at such large distances from the nucleus are rather uncertain, this experiment has little if any practical significance.

V. Calibration stars for the Cerro Tololo plates

To calibrate the surface brightness of the antitail in absolute units, two to three stars have been selected on each photograph. Because of very dense cores of star trails on Curtis-Schmidt plates, only very faint stars, of estimated red magnitudes 13 to 14, can be chosen for calibration. Pursuing a two-step procedure, we first intend to use these stars to calibrate the sky background (at the particular spot on the plate) and then to use the sky background to calibrate the antitail by converting the relative intensities of Tables II to V to absolute units.

Strictly, each calibration star should have been scanned across as well as along its trail. However, inspection of the magnified trails of the calibration stars in a measuring machine has shown that virtually nothing can be gained by scanning the stars along their trails over simply measuring their lengths, once the cross scans are available.

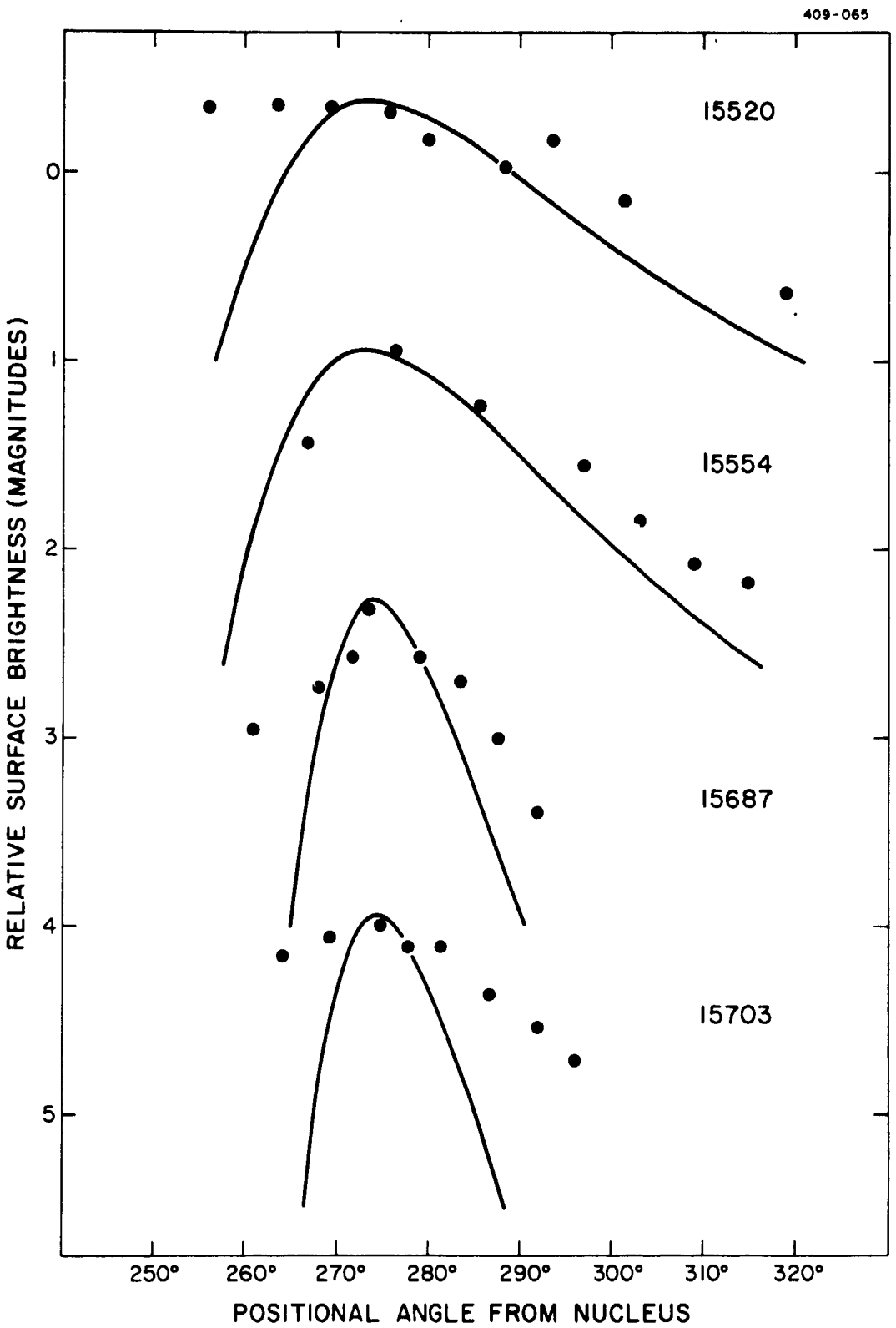

Figure 5. Transverse profiles of the antitail on the Cerro Tololo plates at an angular distance of 20 arcmin from the nucleus. Solid circles: measurements; curves: working model.

To get a meaningful profile of the calibration stars in the direction perpendicular to the trail, a slit diaphragm has been used in the cross scans. The width of the slit in the scanning direction has been fixed at 10 microns (or just below 1 arcsec), a size significantly smaller than the apparent width of the trails of the calibration stars (which is typically 50 microns). To avoid the effect of emulsion granulation, the length of the diaphragm along the trail has been kept at 200 microns (or about 19.3 arcsec), which represents about 10 per cent of an average trail length on the plates. Due to differential refraction, the star trails are not quite straight. Each star was scanned near the middle of its trail and in the direction perpendicular to the tangent to the trail at that point. Differential refraction also affects the measured length of the star trails, which depend, in addition, on the star brightness. An example of a scan of a calibration star is shown in Fig. 6. The photometric reduction of the scans of this type is described in Appendix B and the obtained results are listed in Table VI. The coordinates of the calibration stars - none of which is listed in the SAO catalogue - have been determined by the method of dependences (using up to 10 ambient reference stars) and should be good to within 1 arcsec in each coordinate, except perhaps for the stars on plates 15554, where the accuracy may be somewhat lower. Since the magnitudes of the calibration stars remain to be measured, the calibration cannot be pursued till the end at present. The last column of Table VI gives $H_B - H_*$, the difference between the magnitude per square arcsec H_B of the sky background of relative surface brightness I_B and the magnitude of the calibration star H_*. Both magnitudes should of course refer to the sensitivity profile of the plates with the maximum near 6600Å.

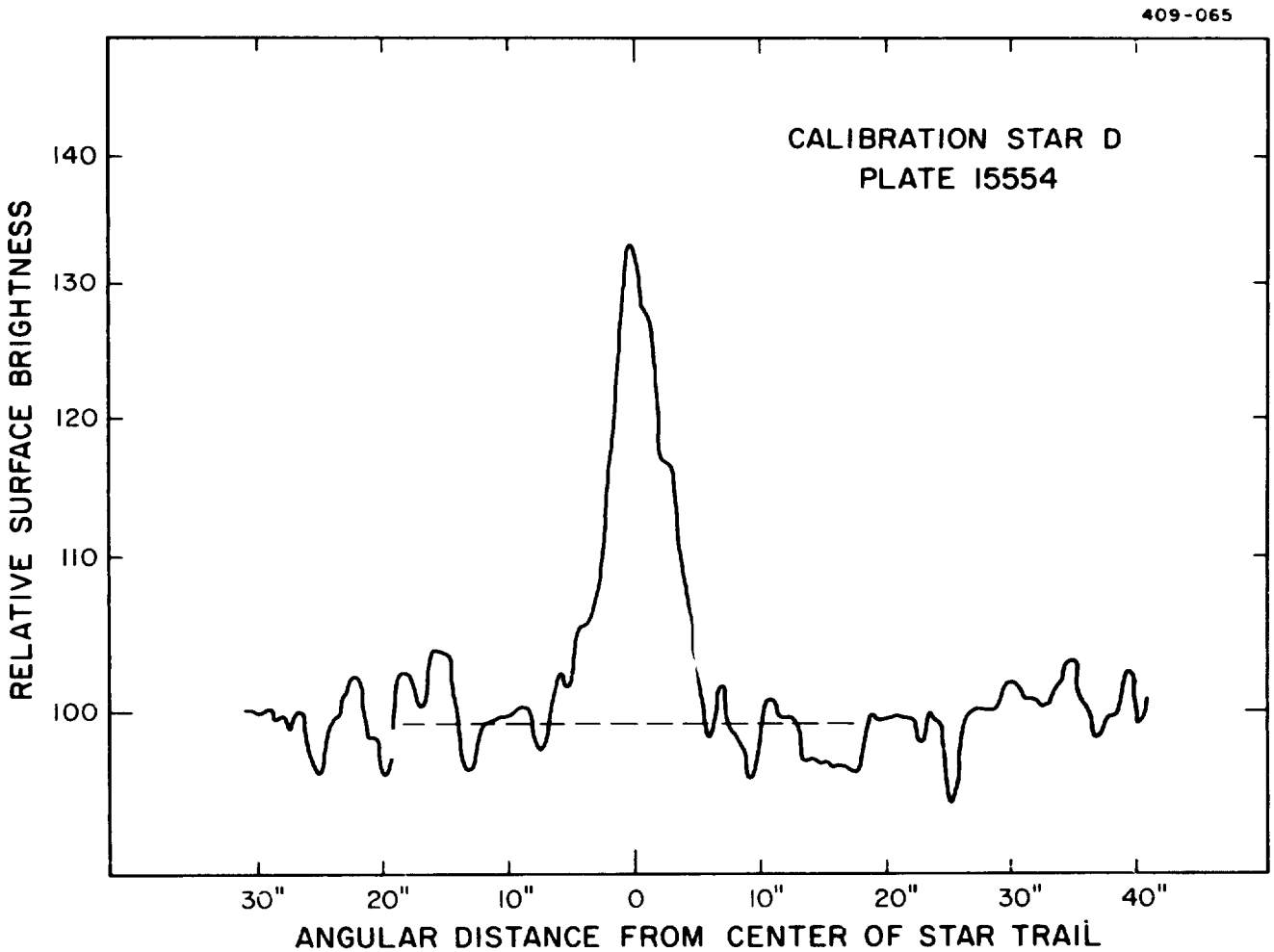

Figure 6. An example of a scan across a calibration star's trail. Scanning slit 1 by 19.3 arcsec; the long side of the slit parallel to the trail. Dashed line: the adopted sky background.

Table VI. Calibration stars for Cerro Tololo plates

Calibration star	Plate	Star's position 1950.0 R.A.	Decl.	Relative brightness of sky background, I_B	Star's peak relative brightness, I_*	Star's width factor, σ	Star's trail length, L	$H_B - H_*$
A	15520	$23^h42^m17^s.90$	+ 0°40'46".8	106.3	43.3 ± 0.3	2".48 ± 0".06	162".5	6^m.5
B	15520	23 44 37.16	+ 0 48 10.7	103.5	60.8 ± 0.3	2.93 ± 0.11	163.5	7.1
C	15554	0 05 53.42	+ 3 18 17.2	100.4	63.8 ± 0.3	2.13 ± 0.04	250.6	7.3
D	15554	0 06 50.05	+ 3 22 55.5	99.2	29.4 ± 0.4	2.36 ± 0.07	249.4	6.6
E	15687	1 53 30.41	+12 13 10.9	106.0	30.3 ± 0.2	3.31 ± 0.12	167.3	6.5
F	15687	1 55 07.83	+12 03 40.8	107.4	42.9 ± 0.5	2.44 ± 0.12	171.6	6.5
G	15703	2 06 01.57	+12 50 32.7	106.3	18.7 ± 0.6	3.01 ± 0.24	151.2	5.7
H	15703	2 06 01.88	+12 50 48.6	106.3	11.3 ± 0.5	3.16 ± 0.20	142.0	5.2
J	15703	2 08 07.86	+13 23 45.5	105.4	27.8 ± 0.5	3.08 ± 0.20	157.6	6.2

VI. Preliminary physical interpretation of the observed radial profiles of the antitail

The progressively increasing gradient of the radial scans is so far the best established property of the antitail. The physical significance of the gradient variations emerges from a relation among the modified surface density of the emitted particles (which is proportional to the relative brightness), their emission flux and size distribution, and the area they occupy in the plane of the sky, as formulated by Finson and Probstein (1968) for small particle-ejection velocities. As long as we consider only large particles, for which the acceleration ratio $1-\mu$ of solar radiation pressure to solar gravity does not exceed ~ 0.01, the relative brightness in a particular direction away from the nucleus can be described by a very simple expression. First, the emission flux is in this case constant, because the radial direction is practically identical with a synchrone. Second, the projected area, occupied by the particles is proportional to $1-\mu$. Third, for a constant particle density the particle diameter δ is inversely proportional to $1-\mu$, because the scattering efficiency of large particles for radiation pressure is practically independent of the particle size. And fourth, the distance R of the large particles from the nucleus is proportional to $1-\mu$. The relative brightness at distance R is then

$$I(R) \sim f(1-\mu)\ (1-\mu)^{-1}, \tag{1}$$

where $f(1-\mu)$ is related to the particle-size distribution function $g(\delta)$ thus:

$$f(1-\mu) \sim \delta^4\ g(\delta) \sim (1-\mu)^{-4} g(\delta). \tag{2}$$

We established in Paper I that there was a relative excess of heavier particles in the antitail, which we interpreted as possible evidence for a significant loss of radius of the dust particles due to evaporation near the perihelion passage. With a sufficient body of observational information we now can test this hypothesis more quantitatively.

Consider an initial (pre-evaporation) distribution function of particle diameters of the form

$$g(\delta)d\delta \sim \delta^{-u}d\delta, \tag{3}$$

where u is a constant. Consider further that, as a result of intense solar heating over a limited period of time, an outer layer $\frac{1}{2}\Delta\delta$ in thickness evaporates away from each particle. This amount is indeed independent of the particle size for material of given structure and composition. A particle of initial diameter δ has now a smaller diameter $\gamma = \delta - \Delta\delta$, and the particle-size distribution (3) changes to

$$g(\gamma)d\gamma \sim (\gamma+\Delta\delta)^{-u}d\gamma. \tag{4}$$

The logarithmic slope of this distribution,

$$t(\gamma) = -\frac{\partial \log_e g(\gamma)}{\partial \log_e \gamma}, \tag{5}$$

depends on diameter γ and is related to the initial exponent u by

$$t(\gamma) = \frac{u}{1 + \frac{\Delta\delta}{\gamma}}. \tag{6}$$

Since $\gamma = C(1-\mu)^{-1}$ (C is a constant and $1-\mu$ now refers to γ rather than to δ), we can write equation (6) as

$$\frac{1}{t} = \frac{1}{u} + \frac{\Delta\delta}{Cu}(1-\mu). \tag{7}$$

On the other hand, we now have $I \sim \gamma^5 g(\gamma)$, so that the radial brightness gradient is

$$w = -\frac{\partial \log_e I(R)}{\partial \log_e R} = -\frac{\partial \log_e I(\gamma)}{\partial \log_e \gamma} \cdot \frac{\partial \log_e \gamma}{\partial \log_e R} = 5 - t(\gamma). \quad (8)$$

Deriving $t(\gamma)$ for a number of angular distances on each of the scanned profiles, assigning the proper value of $1-\mu$ (depending not only on the distance R, but also on the time of observation and on the positional angle of the scan), and plotting the resulting pairs $1-\mu$ vs. $\frac{1}{t}$, we can test the hypothesis of particle evaporation by comparing such a plot with the linear relation predicted by equation (7). The plot, based on the four plates and including only the sections of the antitail where its relative brightness exceeded 2 per cent of the sky background (to avoid unrealistic gradients from very faint areas), is exhibited in Figure 7. A least-square solution indicates a complete absence of nonlinearity (the mean error of the quadratic term came out 4.5 times as large as the term itself), and provides the numerical values of two important characteristics of the population of large dust particles in Comet Kohoutek: exponent u of the initial particle-size distribution [eq. (3)] and the evaporation loss in particle diameter $\Delta\delta$. The two quantities derived from both the separate plates and the whole set are listed in Table VII. The table also includes the population index s of the differential particle-mass distribution $m^{-s}dm$, which relates to the particle-size exponent u of (3),

$$s = \frac{u + 2}{3}, \quad (9)$$

and the acceleration ratio $(1-\mu)_{max}$, corresponding to the largest particles that evaporated completely (i.e., whose $\delta = \Delta\delta$).

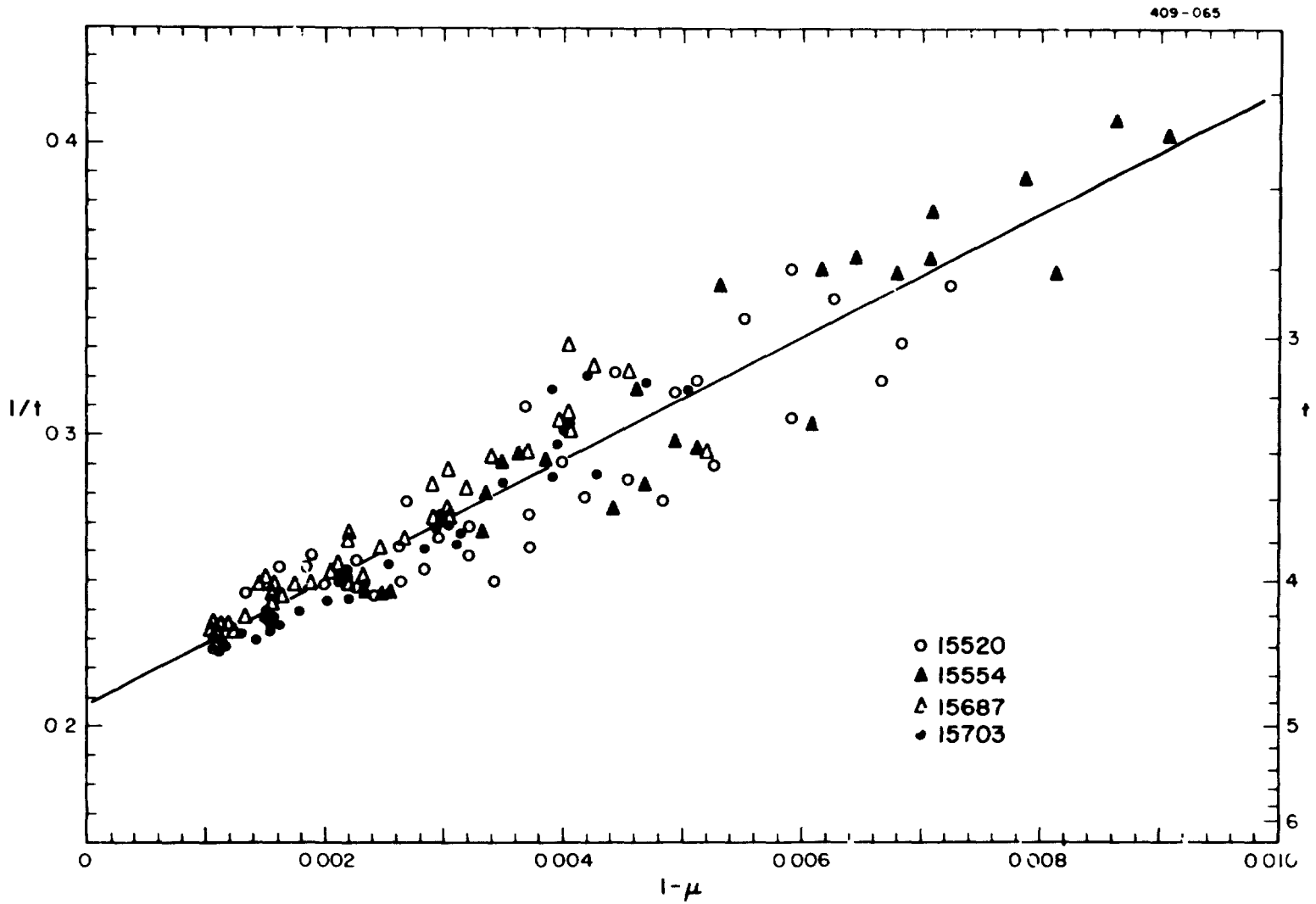

Figure 7. The plot of the particle acceleration 1-μ versus the logarithmic gradient, t, of the size distribution of the vaporizing particles in the antitail.

Table VI. . Characteristics of the dust particles

Plate	Initial size distribution exponent, t	Initial population i· lex, s	Evaporation loss in particle diameter, Δδ (micron)	Initial repulsive force for ıargest completely evaporated particles, $(1-\mu)_{max}$
15520	4.72 ± 0.16	2.24 ± 0.05	103 ± 10	0.0113 ± 0.0011
15554	5.17 ± 0.27	2.39 ± 0.09	142 ± 13	0.0082 ± 0.0007
15687	4.79 ± 0.09	2.26 ± 0.03	131 ± 8	0.0089 ± 0.0005
15703	5.06 ± 0.07	2.35 ± 0.02	147 ± 6	0.0080 ± 0.0003
ALL	4.81 ± 0.06	2.27 ± 0.02	118 ± 4	0.0099 ± 0.0003

Taken at their face value, the data of Table VII appear to indicate rather consistently that the population index is near 2.3 and the size-distribution exponent u near 5, and that only the particles initially larger than 100 to 150 microns in diameter survived the exposure to solar heat. Comparison with Figure 7 of Paper I suggests that the effective vaporization heat of the antitail particles amounts to about 46 kcal/mole. However, there is an uncertainty involved in these results, which is due to the fact that any particle evaporation also affects the particle's future dynamics, because it implies a change in the magnitude of the radiation pressure. Therefore the present results are still preliminary, and the derived loss rate of particle radius due to evaporation may only be an order-of-magnitude estimate. In the improved model of the antitail the dynamical effect of particle evaporation (variable $1-\mu$) must be accounted for.

VII. References

Finson, M. L., and Probstein, R. F. (1968). A theory of dust comets. I. Model and equations. Astrophys. J. 154, 327-352.

Marsden, B.G. (1974). Comet Kohoutek (1973f). IAUC No. 2684.

Sekanina, Z. (1974). On the nature of the antitail of Comet Kohoutek 1973f. I. A working model. Icarus (at press).

PART B. OTHER ACTIVITIES IN THE REPORTED PERIOD

Besides the extensive investigation of the antitail of Comet Kohoutek, the following activities were also undertaken.

1. Computer programs

The package of computer programs, used for the calculation of particle orbits, now works for particle accelerations $1-\mu$ exceeding 1 (negative gravitation), and for both short-period and nearly-parabolic orbits of comets.

2. A general study of the anomalous tails of comets

This study, continued from the previous period, has resulted in a paper "The prediction of anomalous tails of comets", published in Sky and Telescope, vol. 47, pp. 374-377.

3. The anomalous tails of short-period comets

The general rules for the appearance of the anomalous tails have been applied to all the short-period comets of the past; many of these comets should have displayed an anomalous tail on a number of occasions, but no observations of such tails have ever been reported. It is tentatively concluded that the short-period comets fail to emit relatively heavy particles (of a submillimeter and larger size) in significant amounts.

4. The problem of the tails of the distant comets

The results of the hypothesis of the icy tails of the distant comets, proposed in Semiannual Progress Report No. 4 (March 15 to September 14, 1973), has been updated and will be shortly submitted for publication in Icarus under the title "A Study of the Icy Tails of the Distant Comets".

PART C. PLANS FOR THE NEXT PERIOD (SEPTEMBER 15, 1974 TO MARCH 14, 1975)

1. To continue (and complete as soon as possible) the study of the antitail of Comet Kohoutek.

2. To study the antitail of Comet Arend-Roland (1957 III) and to compare the results with those for Comet Kohoutek. Three high-quality photometrically calibrated plates of 1957 III are available from the collection of Dr. F. D. Miller, University of Michigan.

3. To study the motions of dust particles under the effects of evaporation (variable $1-\mu$), and to derive the vaporization parameters (vaporization rate; latent heat of vaporization of the material).

4. To study the synchronic bands in the tails of some comets in terms of the hypothesis of vaporizing particles.

5. To complete (if time allows) the statistical study of the anomalous tails of comets, aimed at our better understanding of the process of ejection of heavy particles from comets.

It is not believed that all the above problems will be completely solved by the end of the next semiannual period. The actual priority to each of the above points of investigation will be assigned during the period so that the whole project is run most efficiently.

In addition, at the invitation of Dr. B. D. Donn, Goddard Space Flight Center, a review paper will be given on the progress in the study of cometary dust tails at the IAU Colloquium No. 25 (Study of Comets), held in late October 1974.

Appendix A. Effects of differential refraction on the distance and directional determinations in the antitail at low altitudes

Because of the sharp increase in the refraction correction of the spherical coordinates at low altitudes, it is desirable to establish the effects of refraction on the distance and directional scales in the antitail.

Let α_1, δ_1 be the refraction-free coordinates of the comet's nucleus, α_2, δ_2 those of a point in the antitail, and similarly α_1', δ_1', α_2', δ_2' the corresponding coordinates affected by refraction. The corrections for refraction are therefore $\Delta\alpha_i = \alpha_i - \alpha_i'$, $\Delta\delta_i = \delta_i - \delta_i'$ $(i = 1,2)$. Since we consider only small arcs, we can write for the refraction-free angular distance Δ of the point (α_2, δ_2) from the nucleus

$$\Delta^2 = [(\alpha_2'+\Delta\alpha_2)-(\alpha_1'+\Delta\alpha_1)]^2\cos^2\tfrac{1}{2}[(\delta_1'+\Delta\delta_1)+(\delta_2'+\Delta\delta_2)]+[(\delta_2'+\Delta\delta_2)-(\delta_1'+\Delta\delta_1)]^2. \quad \text{(A-1)}$$

Denoting the refraction-affected distance of point (α_2, δ_2) as Δ' and realizing that

$$\begin{aligned}
&\cos\tfrac{1}{2}[(\delta_1'+\Delta\delta_1)+(\delta_2'+\Delta\delta_2)] \approx \cos\tfrac{1}{2}[\delta_1'+\delta_2'] \approx \cos\delta_1', \\
&(\alpha_2'-\alpha_1')^2\cos^2\tfrac{1}{2}(\delta_1'+\delta_2')+(\delta_2'-\delta_1')^2 = \Delta'^2, \\
&|\Delta\alpha_2-\Delta\alpha_1| \ll |\alpha_2'-\alpha_1'|, \qquad \text{(A-2)} \\
&|\Delta\delta_2-\Delta\delta_1| \ll |\delta_2'-\delta_1'|, \\
&\Delta^2-\Delta'^2 \approx 2\Delta'(\Delta-\Delta')
\end{aligned}$$

we find the refraction correction in distance to amount to

$$\Delta-\Delta' \doteq \frac{1}{\Delta'}[(\alpha_2'-\alpha_1')(\Delta\alpha_2-\Delta\alpha_1)\cos^2\delta_1'+(\delta_2'-\delta_1')(\Delta\delta_2-\Delta\delta_1)]. \quad \text{(A-3)}$$

Similarly, the refraction-free positional angle p of the point (α_2, δ_2) relative to the nucleus is

$$\tan p = \frac{(\alpha_2'+\Delta\alpha_2)-(\alpha_1'+\Delta\alpha_1)}{(\delta_2'+\Delta\delta_2)-(\delta_1'+\Delta\delta_1)} \cos\tfrac{1}{2}[(\delta_1'+\Delta\delta_1)+(\delta_2'+\Delta\delta_2)]. \quad \text{(A-4)}$$

Because of (A-2), its relation to the refraction-affected positional angle p' is expressed as

$$\tan p \doteq \tan p' \left(1 + \frac{\Delta\alpha_2 - \Delta\alpha_1}{\alpha_2' - \alpha_1'} - \frac{\Delta\delta_2 - \Delta\delta_1}{\delta_2' - \delta_1'}\right), \tag{A-5}$$

and, with p and p' in degrees, the refraction correction in direction becomes

$$p - p' = 28^{\circ}.65 \sin 2p' \left(\frac{\Delta\alpha_2 - \Delta\alpha_1}{\alpha_2' - \alpha_1'} - \frac{\Delta\delta_2 - \Delta\delta_1}{\delta_2' - \delta_1'}\right). \tag{A-6}$$

The corrections $\Delta\alpha_i$, $\Delta\delta_i$ follow from the classical equations of the spherical astronomy:

$$\Delta\alpha_i = -\cos\phi \sin t_i' \sec\delta_i' \operatorname{cosec} z_i' R_i,$$
$$\Delta\delta_i = (\tan\delta_i' \cot z_i' - \sin\phi \sec\delta_i' \operatorname{cosec} z_i') R_i, \tag{A-7}$$

where ϕ is the geographic latitude of the observing place, t_i' and z_i' the hour angle and zenith distance, both refraction-affected, and R the refraction correction in the zenith distance, which, except very near the horizon, can be approximated by

$$R = A \tan z' + B \tan^3 z', \tag{A-8}$$

where A and B are constants.

Appendix B. Photometric calibration of the sky background

We assume that a star's image on a calibrated plate, guided on a moving object (comet), shows up in the form of a trail of length L and characteristic width W (arcsec). We further assume that a photometric scan across a section of the trail is available and that the diaphragm used has been a slit of length ℓ and width w (arcsec), where ℓ<<L and w<<W. Converting the photographic densities across the measured profile of the star to relative intensities and fixing the level of the sky-background noise on the scan, we wish to estimate the contribution of the scanned section of the star to the brightness of the ambient background I_B. We assume that the excess relative intensity I across the star's profile fits a probability-type curve,

$$I(x) = I_* \exp\left[-\frac{(x-x_o)^2}{2\sigma^2}\right], \qquad \text{(B-1)}$$

where x (arcsec) is read from an arbitrary origin x_o, I_* is the peak relative brightness at the center of the star's profile, and σ is the width factor (arcsec). Establishing I(x) for a number of x from the scan we can determine I_* and σ by least squares. Equation (B-1) can be written as

$$\log_e I(x) = A + Bx + Cx^2, \qquad \text{(B-2)}$$

where

$$\left.\begin{aligned} A &= \log_e I_* - \frac{x_o^2}{2\sigma^2} \\ B &= \frac{x_o}{\sigma^2} \\ C &= -\frac{1}{2\sigma^2} \end{aligned}\right\} \qquad \text{(B-3)}$$

so that

$$I_* = \exp\left(A - \frac{B^2}{4C}\right) \qquad \text{(B-4)}$$

and

$$\sigma = (-2C)^{-\frac{1}{2}}. \tag{B-5}$$

The integrated intensity in the scanned section of the star's trail is

$$\int_{-\infty}^{\infty} I \, dx = (2\pi)^{\frac{1}{2}} I_{*} \sigma, \tag{B-6}$$

and the brightness contribution of the whole trail of the star is related to the star's magnitude H_{*}:

$$(2\pi)^{\frac{1}{2}} I_{*} \sigma \frac{L}{\ell} = c. \; 10^{-0.4 H_{*}}, \tag{B-7}$$

where c is a constant. The surface brightness of the ambient sky background H_B (magnitude per square arcsec) can similarly be expressed through the relative brightness I_B and the slit dimensions

$$\frac{I_B}{\ell w} = c. \; 10^{-0.4 H_B}. \tag{B-8}$$

The elimination of c from (B-7) and (B-8) then gives immediately the result:

$$H_B = H_{*} + 2.5 \log_{10} [(2\pi)^{\frac{1}{2}} I_{*} \sigma L w / I_B]. \tag{B-9}$$

Appendix C. Normalized size-density distribution of vaporizing particles

Consider particles, whose diameters δ and densities ρ have originally satisfied a distribution law

$$g(\rho\delta)\, d(\rho\delta) = C_g(\rho\delta)^{-u}\, d(\rho\delta), \tag{C-1}$$

where u and C_g are constants. Consider further that the particles vaporize until their final diameters γ and densities σ are related to the pre-evaporation values thus:

$$\sigma\gamma = \rho\delta - \Delta(\rho\delta), \tag{C-2}$$

where $\Delta(\rho\delta)$ is a constant. Obviously, all the particles for which $\rho\delta < \Delta(\rho\delta)$ vaporize completely, whereas the post-evaporation distribution of the particles with $\rho\delta > \Delta(\rho\delta)$ becomes

$$g(\sigma\gamma)\, d(\sigma\gamma) = C_g\, [\sigma\gamma + \Delta(\rho\delta)]^{-u}\, d(\sigma\gamma). \tag{C-3}$$

In order that this distribution be normalized,

$$\int_0^\infty g(\sigma\gamma)\, d(\sigma\gamma) = 1, \tag{C-4}$$

the constant C_g must satisfy the relation

$$C_g = (u - 1)\, [\Delta(\rho\delta)]^{u-1}. \tag{C-5}$$

The distribution of radiation-pressure accelerations $1-\mu$, associated with the particle size-density distribution (C-3) is

$$f(1-\mu)\, d(1-\mu) = C_f'\, (\sigma\gamma)^4\, g(\sigma\gamma)\, d(1-\mu), \tag{C-6}$$

or because $\sigma\gamma = C(1-\mu)^{-1}$

$$f(1-\mu)\, d(1-\mu) = C_f\, \left(\frac{1-\mu}{C}\right)^{u-4} \cdot \left[1 + \frac{1-\mu}{(1-\mu)_{max}}\right]^{-u} d(1-\mu), \tag{C-7}$$

where $C_f = C_f' \cdot C_g$ and $(1-\mu)_{max}$ is the radiation-pressure acceleration exerted on the largest particles that later evaporated completely [$\rho\delta = \Delta(\rho\delta)$].

Normalizing distribution (C-7) we obtain

$$C_f = 3 \binom{u-1}{3} (1-\mu)_{max}^{3-u} \cdot C^{u-4}, \qquad \text{(C-8)}$$

so that

$$f(1-\mu)\, d(1-\mu) = 3 \binom{u-1}{3} (1-\mu)_{max}^{3-u} (1-\mu)^{u-4} \left[1 + \frac{1-\mu}{(1-\mu)_{max}}\right]^{-u}. \qquad \text{(C-9)}$$

Finally, the important parameter appearing in the expression for the mass-loss rate of the dust and numerically equal to the ratio of the mean cube to the mean square of the size-density distribution [see eqs. (8) and (10) of Paper I], becomes

$$\overline{(\sigma\gamma)^3} / \overline{(\sigma\gamma)^2} = \frac{3C}{(u-4)\ (1-\mu)_{max}} = \frac{3\ \Delta(\rho\delta)}{u-4} \quad . \qquad \text{(C-10)}$$